

Radial interchange motions of plasma filaments

O. E. Garcia, N. H. Bian, and W. Fundamenski

Citation: *Physics of Plasmas* **13**, 082309 (2006); doi: 10.1063/1.2336422

View online: <https://doi.org/10.1063/1.2336422>

View Table of Contents: <http://aip.scitation.org/toc/php/13/8>

Published by the [American Institute of Physics](#)

Articles you may be interested in

[Convective transport by intermittent blob-filaments: Comparison of theory and experiment](#)

Physics of Plasmas **18**, 060501 (2011); 10.1063/1.3594609

[Mechanism and scaling for convection of isolated structures in nonuniformly magnetized plasmas](#)

Physics of Plasmas **12**, 090701 (2005); 10.1063/1.2044487

[Transport by intermittency in the boundary of the DIII-D tokamak](#)

Physics of Plasmas **10**, 1670 (2003); 10.1063/1.1563259

[Blob birth and transport in the tokamak edge plasma: Analysis of imaging data](#)

Physics of Plasmas **13**, 092509 (2006); 10.1063/1.2355668

[Transport by intermittent convection in the boundary of the DIII-D tokamak](#)

Physics of Plasmas **8**, 4826 (2001); 10.1063/1.1406940

[Particle transport in the scrape-off layer and its relationship to discharge density limit in Alcator C-Mod](#)

Physics of Plasmas **8**, 2107 (2001); 10.1063/1.1352596

PHYSICS TODAY

WHITEPAPERS

MANAGER'S GUIDE

Accelerate R&D with
Multiphysics Simulation

READ NOW

PRESENTED BY

 COMSOL

Radial interchange motions of plasma filaments

O. E. Garcia^{a)}

Association EURATOM-Risø National Laboratory, P.O. Box 49, OPL-128 Risø, DK-4000 Roskilde, Denmark

N. H. Bian

School of Physics and Astronomy, The University of Manchester, Manchester M60 1QD, United Kingdom

W. Fundamenski

EURATOM/UKAEA Fusion Association, Culham Science Centre, Abingdon OX14 3DB, United Kingdom

(Received 11 April 2006; accepted 29 June 2006; published online 29 August 2006)

Radial convection of isolated filamentary structures due to interchange motions in magnetized plasmas is investigated. Following a basic discussion of vorticity generation, ballooning, and the role of sheaths, a two-field interchange model is studied by means of numerical simulations on a biperiodic domain perpendicular to the magnetic field. It is demonstrated that a blob-like plasma structure develops dipolar vorticity and electrostatic potential fields, resulting in rapid radial acceleration and formation of a steep front and a trailing wake. While the dynamical evolution strongly depends on the amount of collisional diffusion and viscosity, the structure travels a radial distance many times its initial size in all parameter regimes in the absence of sheath dissipation. In the ideal limit, there is an inertial scaling for the maximum radial velocity of isolated filaments. This velocity scales as the acoustic speed times the square root of the structure size relative to the length scale of the magnetic field. The plasma filament eventually decelerates due to mixing and collisional dissipation. Finally, the role of sheath dissipation is investigated. When included in the simulations, it significantly reduces the radial velocity of isolated filaments. The results are discussed in the context of convective transport in scrape-off layer plasmas, comprising both blob-like structures in low confinement modes and edge localized mode filaments in unstable high confinement regimes.

© 2006 American Institute of Physics. [DOI: [10.1063/1.2336422](https://doi.org/10.1063/1.2336422)]

I. INTRODUCTION

Radial transport of particles and heat in the scrape-off layer (SOL) of magnetically confined plasmas is generally found to be turbulent and dominated by the motion of field-aligned *filaments*, appearing as *blobs* in the plane perpendicular to the magnetic field, with a radial velocity component being a significant fraction of the acoustic speed.^{1–20} This turbulent radial transport is believed to be the cause of the experimentally observed broad particle density profiles and large relative fluctuation levels throughout the SOL, and hence to strongly influence the level of plasma-wall interactions.^{21–27} Moreover, the ballooning character of the radial turbulent transport into the SOL may drive strong parallel plasma flows, which also influences divertor operation and material migration.^{17–27} Recent observations of strong filamentary structures in the SOL in association with edge localized mode (ELM) activity have many similarities with the blob structures observed in low confinement modes, indicating that they might be governed by the same physical mechanisms.^{28–43} It is evident that a detailed understanding of the collective dynamics in the plasma boundary region would help to provide a basis for efficient operation of the next-generation fusion experiments.

Large-scale motion of localized structures driven by interchange dynamics is a well-known phenomenon for both

fluids and magnetized plasmas. In nonuniformly heated ordinary fluids in a gravitational field, thermal convection may lead to the formation of structures known as *plumes* or *thermals* that travel in the direction of buoyancy.^{44–48} Another well known example is the phenomenon that takes place during ionospheric irregularities where localized regions of plasma depletions, often referred to as *bubbles*, move radially outwards on the night-side of the equatorial *F* layer ionosphere.^{49–52} In all such cases, localized structures may move into regions that are locally stable to interchange motions, an example of which is known as penetrative convection.^{53–55} As will be discussed in this paper, turbulent transport at the boundary of magnetically confined plasmas may also be fruitfully considered within this context. Indeed, the physical mechanism is the same for all these systems.

The mechanisms underlying radial motion of filamentary structures in the SOL of magnetically confined plasmas have recently become a subject of substantial investigation. Most of this work has been based on the presumption of electrostatic sheaths at limiters or divertor target plates.^{56–65} The interchange drive due to the nonuniform magnetic field was assumed to be balanced by parallel currents to the sheaths, implicitly assuming perfectly field-aligned plasma perturbations in the region of open magnetic-field lines. In the simplest description, this yields an analytical “blob solution” predicting a uniform radial velocity of filamentary structures scaling inversely proportional to both the sheath dissipation coefficient and the square of the structure size perpendicular

^{a)}Electronic mail: odd.erik.garcia@risoe.dk

to the magnetic field.^{57–62} Numerical simulations that included inertial effects verified the radial transport property of isolated structures, but no systematic parameter investigations have been performed thus far.^{60–64}

In this contribution, we reconsider the problem of radial convection of isolated filament structures by electrostatic interchange motions. Partly motivated by the numerous experimental observations of ballooning in the fluctuation level and turbulent transport, we investigate a simplified two-field model governing the interchange dynamics on the outer mid-plane of toroidally magnetized plasmas. The evolution of a thermodynamic variable is modeled by a simple advection-diffusion equation, while the equation for the convective flow dynamics arises from electric current continuity involving polarization due to inertia, interchange drive due to the non-uniform magnetic field, and viscous stresses. It is shown that the inertial response to the interchange drive is the salient mechanism that leads to radial motion of isolated structures, without any presumptions of plasma sheaths.^{66,67}

Radial motion of a blob structure initially at rest follows from the formation of dipolar vorticity and electrostatic potential fields. The plasma filament accelerates rapidly and develops a steep front and a trailing wake. The latter is a characteristic feature of all experimental probe measurements.^{1–13} Depending on the strength of collisional diffusion and viscosity, the structure may undergo significant distortions due to stretching and mixing by the convective motions. Nevertheless, in all parameter regimes the structure travels a radial distance many times its initial size. An inertial velocity scaling is derived in the ideal limit, predicting a maximum radial velocity relative to the acoustic speed scaling as the square root of the structure size relative to the length scale of the magnetic field. This velocity scaling is recovered by numerical simulations. A systematic parameter investigation for the simulations is presented, elucidating the importance of collisional diffusion and viscosity for the radial motion and dispersion of blob structures.

Finally, the role of parallel currents to plasma sheaths is investigated by adding the conventional sheath dissipation term to the charge continuity equation. The resulting model is similar to that used in the previous theories of radial structure motion.^{56–65} By means of numerical simulations, it is demonstrated that the presence of sheath dissipation strongly reduces the radial center-of-mass velocity of isolated structures. One may conclude that the radial motion of filamentary structures in the region of open magnetic-field lines occurs due to a combination of vorticity or charge polarization caused by magnetic guiding center drifts and the ensuing large-scale convective flow associated with plasma inertia. Accordingly, there is an intrinsic dynamical evolution of the blob structures that compares favorably with experimental measurements.

This article is organized as follows. In the following section, we describe the physical mechanism of radial structure motion by interchange dynamics in a nonuniformly magnetized plasma. The physics of vorticity generation, ballooning, and sheath currents is briefly reviewed. In Sec. III we present the reduced two-field model equations used in this work, the normalization, boundary, and initial conditions, and the

center-of-mass moments used for diagnosing the numerical simulations. Analytical blob velocity scalings are derived and the effect of sheath dissipation is discussed. Results from a series of numerical simulations are presented in Sec. IV demonstrating acceleration, front formation, and dispersion of isolated blob structures. The dependence of the dynamical evolution on collisional diffusion, viscosity, and sheath dissipation is analyzed by means of center-of-mass coordinates. A discussion of the results in the context of intermittent SOL transport and ELM dynamics is given in Sec. V, and finally a summary and our conclusions are given in Sec. VI. This is a continuation of our previous work presented in Refs. 66 and 67.

II. INTERCHANGE MOTIONS

In this section, a general discussion is given of interchange motions due to a nonuniform magnetic field and its relation to the experimentally observed ballooning in the fluctuation level and the turbulent transport at the boundary of toroidally magnetized plasmas. The role of parallel motions and electric currents in the SOL is also briefly described.

A. Vorticity generation

An equation describing momentum conservation for a quasineutral plasma in a magnetic field \mathbf{B} in model-independent form is given by

$$\rho \left(\frac{\partial}{\partial t} + \mathbf{V} \cdot \nabla \right) \mathbf{V} + \nabla \cdot \Pi = \mathbf{J} \times \mathbf{B} - \nabla P, \quad (1)$$

where Π represents the deviation of the plasma stress tensor from the diagonal scalar pressure P , ρ is the plasma mass density, and \mathbf{J} is the electric current density. We further define the magnetic-field unit vector $\mathbf{b} = \mathbf{B}/B$ and curvature vector $\boldsymbol{\kappa} = (\mathbf{b} \cdot \nabla) \mathbf{b}$. Denoting the left-hand side of Eq. (1) by \mathbf{F} and taking the curl gives the exact field-aligned component of the plasma vorticity equation,⁶⁸

$$\mathbf{b} \cdot (\nabla \times \mathbf{F} - 2\boldsymbol{\kappa} \times \mathbf{F}) = BB \cdot \nabla \left(\frac{J_{\parallel}}{B} \right) + 2\mathbf{b} \cdot \boldsymbol{\kappa} \times \nabla P. \quad (2)$$

The left-hand side of this equation describes plasma inertia, predominantly involving the rate of change of the curl of the electric drift $\mathbf{V}_E = \mathbf{b} \times \nabla \phi / B$, and thus the plasma response to the driving forces on the right-hand side. Notably, in the last term on the right-hand side, only perpendicular pressure gradients in combination with magnetic-field curvature appear as a source of vorticity.

Equation (2) may also be interpreted as one of current continuity, with the left-hand side resulting from the divergence of the polarization current, which to lowest order is given by

$$\mathbf{J}_p = \frac{\rho}{B} \mathbf{b} \times \left(\frac{\partial}{\partial t} + \mathbf{V}_E \cdot \nabla \right) \mathbf{V}_E. \quad (3)$$

The divergence of this current density yields the rate of change of the electric drift vorticity $\boldsymbol{\Omega} = \mathbf{b} \cdot \nabla \times \mathbf{V}_E$. The two terms on the right-hand side of Eq. (2) describe the compres-

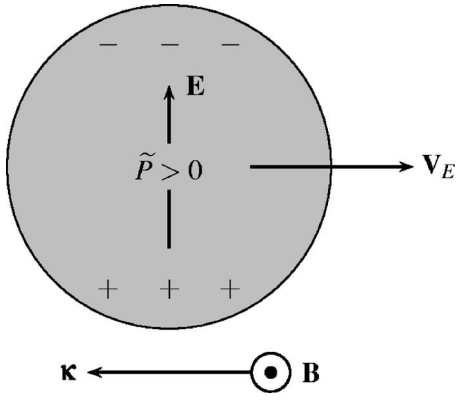


FIG. 1. Illustration of the ideal interchange mechanism leading to radial motion of a localized blob structure with an excess pressure \tilde{P} relative to the ambient plasma. The vertical polarization of electric charge and vorticity due to magnetic guiding center drifts leads to a radial electric drift at the center of the blob structure.

sion of parallel and diamagnetic currents, respectively. The latter is defined by $\mathbf{J}_d = \mathbf{b} \times \nabla P / B$ and represents the drive of interchange motions in nonuniformly magnetized plasmas. From the electric current densities defined above, the charge continuity equation for the quasineutral plasma might be written as $\nabla \cdot \mathbf{J}_p = -\nabla \cdot \mathbf{J}_\parallel - \nabla \cdot \mathbf{J}_d$, which corresponds term by term to the vorticity equation (2).

The physics of vorticity generation and interchange motions in nonuniformly magnetized plasmas is described by Eq. (2). An illustration of this mechanism is presented in Fig. 1 for a plasma blob with pressure perturbation $\tilde{P} > 0$. We note that the electric current density due to magnetic guiding center drifts in a nonuniform magnetic field is given by⁶⁹

$$\mathbf{J}_B = \frac{P}{B} (\nabla \times \mathbf{b} + \mathbf{b} \times \nabla \ln B), \quad (4)$$

comprising the effects of magnetic-field curvature and inhomogeneity. With reference to Fig. 1, this current causes a vertical charge separation due to accumulation of charged particles of a definite sign in regions with a vertical pressure gradient. In the fluid description, this is described by the diamagnetic current compression,

$$\nabla \cdot \mathbf{J}_d = \frac{1}{B} (\nabla \times \mathbf{b} + \mathbf{b} \times \nabla \ln B) \cdot \nabla P = \nabla \cdot \mathbf{J}_B, \quad (5)$$

where the two terms inside the parentheses contribute equally in the electrostatic limit. It should be noted that there is no net vorticity generation by this interchange mechanism; it only acts to polarize electric charge and thus vorticity when the magnetic guiding center drifts of negatively and positively charged particles do not balance. The charge polarization gives rise to a vertical electric field and hence a radial electric drift at the center of the blob structure. When this dipolar charge separation is dynamically balanced by the polarization current, the result is a large-scale convective flow field and hence a net radial acceleration and motion of a blob structure initially at rest.^{66,67}

B. Ballooning and parallel flows

The energy conservation equation for reduced fluid descriptions is obtained by multiplying the current continuity equation (2) with the electrostatic potential ϕ and integrating over space.^{70–73} The polarization current term on the left-hand side then to lowest order yields the temporal rate of change of the fluid kinetic energy based on the electric drift,

$$- \int d\mathbf{x} \phi \nabla \cdot \mathbf{J}_p = \frac{d}{dt} \int d\mathbf{x} \frac{1}{2} \rho \mathbf{V}_E^2, \quad (6)$$

where the integration extends over the plasma layer under consideration. The diamagnetic current compression on the right-hand side of Eq. (2) gives an energy transfer term for the electric drift kinetic energy,

$$- \int d\mathbf{x} \phi \nabla \cdot \mathbf{J}_d = \int d\mathbf{x} P \nabla \cdot \mathbf{V}_E = \int d\mathbf{x} 2P \mathbf{V}_E \cdot \boldsymbol{\kappa}, \quad (7)$$

assuming the surface term to vanish after integration by parts. It is thus clear that cross-field plasma motions are amplified provided the collective thermal energy flux is directed opposite to the magnetic-field curvature vector. For a plasma in a toroidal magnetic field, this is along the major radius axis, thus implying ballooning of the fluctuation level and the turbulent transport, that is, they tend to maximize on the outer midplane, often referred to as the side of unfavorable magnetic curvature. As a result, plasma and heat enter the region of open magnetic-field lines predominantly on the outer midplane.^{16–20}

The poloidally asymmetric transport of plasma into the SOL caused by ballooning can induce parallel plasma flows in the SOL due to particle transport along the field lines. Such transport-driven parallel flows would be independent of the direction of the magnetic field, in contrast to neoclassical flows and toroidal rotation. Measurements during experiments with forward and reversed magnetic-field directions as well as discharges with different magnetic topologies have clearly indicated the existence of such transport-driven parallel flows.^{17–20} Apart from its direct interest for divertor operation, the observation of ballooning and associated parallel flows strongly suggests interchange motions as the mechanism governing the collective dynamics and cross-field transport in the plasma boundary region.

C. Sheath dissipation

Modeling the behavior of a plasma at material surfaces is very challenging, and usually involves a large number of approximations. In the very simplest cases this can, however, be treated within a fluid description. Assuming Boltzmann distributed electrons and the plasma facing surface to be electrically floating, the boundary condition for the parallel electric currents at the sheaths is given by

$$J_\parallel = -enC_s \left[1 - \exp\left(-\frac{e\phi}{T}\right) \right] \hat{\mathbf{n}} \cdot \mathbf{b}, \quad (8)$$

where ϕ is the deviation of the electric plasma potential from its stationary floating value with respect to the surface potential and $\hat{\mathbf{n}}$ is the surface unit normal vector. Moreover, n and

T are the electron particle density and temperature, respectively, and C_s is the acoustic speed. In the following, we briefly outline how such sheath currents enter the vorticity dynamics and energetics of SOL plasmas.

The effect of parallel currents on the collective plasma dynamics is clearly described by the second term on the right-hand side of Eq. (2). Neglecting parallel gradients in the magnetic-field strength, we have $\nabla \cdot \mathbf{J}_{\parallel} = \mathbf{b} \cdot \nabla J_{\parallel}$. We further define an average over the parallel direction with a connection length of L_{\parallel} by

$$\langle \cdot \rangle = \frac{1}{2L_{\parallel}} \int_{-L_{\parallel}}^{L_{\parallel}} ds, \quad (9)$$

where s is a coordinate along the magnetic-field lines. Using the sheath boundary condition in Eq. (8), the average of the divergence of the parallel current compression becomes

$$\langle \mathbf{b} \cdot \nabla J_{\parallel} \rangle = \frac{enC_s}{L_{\parallel}} \left[1 - \exp\left(-\frac{e\phi}{T}\right) \right], \quad (10)$$

since the electric current is oppositely directed at the two ends where a field line intersects the material surface. A simplified description of the effect of sheath currents on the collective plasma dynamics is thus obtained by averaging the model equations along the field lines. One thereby obtain two-dimensional model equations describing the dynamics of field-aligned structures in the drift plane perpendicular to the magnetic field. The energetic effect of such sheath currents is given by the rate of change of the fluid kinetic energy described in Eq. (6). Under the sheath-connected approximation, this becomes

$$\int d\mathbf{x} \phi \langle \nabla \cdot \mathbf{J}_{\parallel} \rangle = \int d\mathbf{x} \frac{PC_s}{L_{\parallel}} \frac{e\phi}{T} \left[1 - \exp\left(-\frac{e\phi}{T}\right) \right]. \quad (11)$$

Since the integrand on the right-hand side is a non-negative function, it is clear that sheath currents provide a sink for the kinetic energy of the fluctuating motions. Further implications of this effective ‘‘sheath dissipation’’ will be given in Sec. III C.

There are several limitations to this conventional approximation for sheath currents. First of all, the parallel averaging operator generally does not commute with the nonlinear advection terms since the latter involve fluctuations with finite parallel correlation lengths. We further note that the sheath-limited approximation does not comply with the observed ballooning and transport-driven parallel flows. Finally, the assumption of a sheath-connected plasma implies that it should be collisionless, while tokamak SOL plasmas often have significant collisionality. These circumstances motivate an investigation of interchange motions without taking into account the effects of sheath currents.

III. INTERCHANGE MODEL

Based on the basic considerations presented above, this section introduces a paradigmatic two-field model for the nonlinear evolution of interchange motions. This is followed

by a discussion of the center-of-mass coordinates, velocity scalings, and the effect of sheath dissipation for the radial motion of an isolated blob structure.

A. Reduced model equations

In the remaining part of this work, we will investigate the mechanisms for motion and dispersion of isolated blob structures described by a simple interchange model that is based on the general vorticity equation (2). Until further notice, the effect of parallel currents will be neglected, and the lowest-order cross-field plasma motion is assumed to be dominated by the electric drift. Invoking the thin layer approximation and hence local slab coordinates x , y , and z in the radial, poloidal, and local magnetic-field directions, respectively, the vorticity equation (2) reduces to

$$\left(\frac{\partial}{\partial t} + \frac{1}{B} \hat{\mathbf{z}} \times \nabla \phi \cdot \nabla \right) \Omega + \frac{2}{\rho R} \frac{\partial P}{\partial y} = \eta \nabla_{\perp}^2 \Omega, \quad (12)$$

where the last term on the left-hand side describes the interchange drive due to compression of the diamagnetic current in the nonuniform magnetic field with radius of curvature R . Moreover, η is the kinematic viscosity and the electric drift vorticity is $\Omega = \nabla_{\perp}^2 \phi / B$.

A closed model is obtained from the equations governing the thermodynamic variables ρ and P . Here we will consider the simplest case of a two-field model by taking into account the dynamical evolution of only one thermodynamic variable denoted by θ . This may correspond to either the plasma density or pressure, the two limits corresponding to an isothermal plasma and reduced magnetohydrodynamics, respectively. In either case, the structure of the vorticity equation is the same. The simplest possible self-consistent transport problem is thus settled by assuming an advection-diffusion equation for a generic thermodynamic variable,

$$\left(\frac{\partial}{\partial t} + \frac{1}{B} \hat{\mathbf{z}} \times \nabla \phi \cdot \nabla \right) \theta = \chi \nabla_{\perp}^2 \theta, \quad (13)$$

where χ is the collisional diffusivity. Adding effects due to electric drift compressibility and diamagnetic drifts to this equation increases the parameter space while the qualitative behavior remains the same. In the following, we thus consider this two-field model, which describes the nonlinear evolution of interchange motions.^{74–81}

Normalizing spatial scales by a characteristic cross-field blob size ℓ , temporal scales by the corresponding ideal interchange time $1/\gamma$, and thermodynamic perturbations with a characteristic variation $\Delta\theta$, the nondimensional model equations may be written as

$$\left(\frac{\partial}{\partial t} + \hat{\mathbf{z}} \times \nabla \phi \cdot \nabla \right) \theta = \kappa \nabla_{\perp}^2 \theta, \quad (14a)$$

$$\left(\frac{\partial}{\partial t} + \hat{\mathbf{z}} \times \nabla \phi \cdot \nabla \right) \Omega + \frac{\partial \theta}{\partial y} = \mu \nabla_{\perp}^2 \Omega, \quad (14b)$$

where θ is the deviation of the thermodynamic variable from a uniform background Θ , and κ and μ are the nondimensional diffusion and viscosity coefficients, respectively. The

last term on the left-hand side of Eq. (14b) describes the interchange drive due to a nonuniform magnetic field, with the ideal interchange rate given by

$$\gamma = \left(\frac{g \Delta \theta}{\ell \Theta} \right)^{1/2}. \quad (15)$$

Here we have introduced the effective gravity $g = 2C_s^2/R$ and the acoustic speed $C_s = (P/\rho)^{1/2}$. The model equations (14) are identical to those describing two-dimensional thermal convection in a thin fluid layer. We hence identify the corresponding Rayleigh and Prandtl numbers, given by

$$\text{Ra} = \frac{1}{\kappa \mu}, \quad \text{Pr} = \frac{\mu}{\kappa}, \quad (16)$$

respectively. In terms of the dimensional parameters these may be written as

$$\text{Ra} = \frac{g \ell^3 \Delta \theta}{\chi \eta \Theta}, \quad \text{Pr} = \frac{\eta}{\chi}. \quad (17)$$

The Rayleigh number is simply the ratio of effective buoyancy to dissipative forces. Significantly, the Rayleigh number increases linearly with the relative amplitude of the blob structure and as the cube of its spatial size, while the Prandtl number measures the relative strength of viscosity and diffusion. In Sec. IV, we will use these two numbers in order to map out the parameter dependence of blob motion and dispersion.

B. Advection and dispersion

A comprehensive numerical study of the interchange model (14) has been undertaken. The simulations are all initialized with a symmetric blob structure for the thermodynamic variable centered at the origin of the coordinate system,

$$\theta(\mathbf{x}, t=0) = \exp\left(-\frac{1}{2}\mathbf{x}^2\right). \quad (18)$$

It should be noted that, consistent with the normalization stated above, the initial condition (18) has an amplitude and length scale of unity. Initially there is no flow field, which hence follows from the polarization of vorticity by the blob structure described by the last term on the left-hand side of Eq. (14b). Plasma blobs will thus travel radially outwards, while plasma depletions will move radially inwards with respect to the major torus axis. Note that, due to the absence of free-energy sources, the asymptotic state is that of thermodynamic equilibrium with the initial blob structure distributed uniformly in space. Indeed, in the absence of convective motions, the solution of the diffusion equation with the initial condition (18) on an infinite domain is given by

$$\theta(\mathbf{x}, t) = \frac{1}{1 + 2\kappa t} \exp\left[-\frac{\mathbf{x}^2}{2(1 + 2\kappa t)}\right]. \quad (19)$$

Here we will study the transient dynamics leading to thermodynamic equilibrium and the associated convective transport and dispersion of the blob structure given by Eq. (18).

In order to investigate the dynamics of isolated structures, periodic boundary conditions are invoked for the drift plane perpendicular to the magnetic field. Consequently, the integral

$$Q = \int d\mathbf{x} \theta \quad (20)$$

is a conserved quantity, where the integration extends over the bi-periodic domain. A quantitative description of the motion of blob structures is given by the center-of-mass coordinates, defined by

$$X_c = \frac{1}{Q} \int d\mathbf{x} x \theta, \quad Y_c = \frac{1}{Q} \int d\mathbf{x} y \theta, \quad (21)$$

and the corresponding center-of-mass velocity components,

$$V_x = \frac{dX_c}{dt}, \quad V_y = \frac{dY_c}{dt}. \quad (22)$$

The evolution of the radial center-of-mass coordinate X_c gives information about the net radial motion of an initially localized blob structure, with the magnitude measured with respect to the initial structure size. Multiplying Eq. (14a) with the radial coordinate and integrating over space, it is straightforward to show that the radial center-of-mass velocity is proportional to the total radial convective flux,

$$V_x = -\frac{1}{Q} \int d\mathbf{x} \theta \frac{\partial \phi}{\partial y}. \quad (23)$$

It follows that all the properties of the convective flux due to an isolated plasma filament are given by the radial center-of-mass velocity, which is thus a quantity of great interest and investigated in detail in the following. Let us also remark that the kinetic energy integral of the interchange model (14) evolves according to

$$\frac{d}{dt} \int d\mathbf{x} \frac{1}{2} (\nabla_{\perp} \phi)^2 = - \int d\mathbf{x} \theta \frac{\partial \phi}{\partial y} - \mu \int d\mathbf{x} \Omega^2. \quad (24)$$

This clearly shows that radial convective transport appears as a transient source for the fluctuating motions, as discussed more generally in Sec. II B.

In the ideal limit, a simple balance of terms in the vorticity equation (12) immediately reveals an inertial scaling for the velocity, $V \sim 1$, which in dimensional units becomes

$$\frac{V}{C_s} \sim \left(\frac{2\ell \Delta \theta}{R \Theta} \right)^{1/2}. \quad (25)$$

Notably, this is the only allowable scaling according to dimensional analysis in the absence of dissipation. The inertial scaling given by Eq. (25) predicts a blob velocity relative to the acoustic speed, which is given solely by the magnetic-field length scale and the structure size and relative amplitude. Numerical simulations presented in Sec. IV support this as the relevant scaling for the maximum blob velocity.

Mixing of the initially localized blob structure by the interchange motions may alter the correlations and bring the radial advection to a halt. We thus define the relative dispersion tensor components

$$W_{xx} = \frac{1}{Q} \int d\mathbf{x} \theta (x - X_c)^2, \quad W_{yy} = \frac{1}{Q} \int d\mathbf{x} \theta (y - Y_c)^2, \quad (26)$$

describing spreading or mixing of the blob structure relative to the center-of-mass coordinates due to collisional diffusion and the convective motions. Formally, we may relate the diagonal dispersion tensor elements to effective diffusivities, defined by

$$D_x = \frac{1}{2} \frac{dW_{xx}}{dt}, \quad D_y = \frac{1}{2} \frac{dW_{yy}}{dt}. \quad (27)$$

If these diffusivities are constant, the relative dispersion tensor elements W_{xx} and W_{yy} can be approximated by $2D_x t$ and $2D_y t$, respectively. In Sec. IV these expressions will be used to describe the dispersion of the blob structure for different parameter regimes.

C. Sheath dissipation

Including the effect of sheath currents in the region of open magnetic-field lines, discussed in Sec. II C, the nondimensional model equations become

$$\left(\frac{\partial}{\partial t} + \hat{\mathbf{z}} \times \nabla \phi \cdot \nabla \right) \theta = \kappa \nabla_{\perp}^2 \theta, \quad (28a)$$

$$\left(\frac{\partial}{\partial t} + \hat{\mathbf{z}} \times \nabla \phi \cdot \nabla \right) \Omega + \frac{\partial \theta}{\partial y} = \mu \nabla_{\perp}^2 \Omega + \Lambda \phi, \quad (28b)$$

where we have assumed small electrostatic potential fluctuations by linearizing the exponential function in the sheath dissipation term in Eq. (10). The nondimensional sheath dissipation parameter is given by

$$\Lambda = \frac{2C_s \ell^2}{\gamma L_{\parallel} \rho_s^2}, \quad (29)$$

where $\rho_s = C_s / \omega_{ci}$ is the hybrid thermal gyroradius. The basic effect of the various terms in the vorticity equation (28b) is elucidated by a spectral decomposition, which for the linearized equation yields

$$\frac{d\hat{\phi}_{\mathbf{k}}}{dt} = \frac{ik_y}{k_{\perp}^2} \hat{\theta}_{\mathbf{k}} - \mu k_{\perp}^2 \hat{\phi}_{\mathbf{k}} - \frac{\Lambda}{k_{\perp}^2} \hat{\phi}_{\mathbf{k}}. \quad (30)$$

The terms on the right-hand side reveal the essence of the different physical processes. The interchange drive described by the first term imposes a phase shift that causes radial convective transport. The second term shows that viscosity damps small spatial length scales, while the third term shows that sheath currents tend to linearly damp large spatial length scales in the flow field. As will be seen in the following section, the sheath damping of large spatial length scales has profound influences on the motion and dispersion of isolated blob structures.

In most previous theories of radial structure motion in SOL plasmas, the model was formulated in terms of the particle density, and the interchange term from Eq. (12) was taken to be nonlinear in θ ,

$$\left(\frac{\partial}{\partial t} + \hat{\mathbf{z}} \times \nabla \phi \cdot \nabla \right) \Omega + \frac{1}{\theta} \frac{\partial \theta}{\partial y} = \mu \nabla_{\perp}^2 \Omega + \Lambda \phi. \quad (31)$$

This form of the vorticity equation formally allows an analytical solution in the absence of collisional diffusion and viscosity,^{57–62}

$$\theta(\mathbf{x}, t) = \vartheta \left(x - \frac{t}{\Lambda} \right) \exp \left(-\frac{1}{2} y^2 \right), \quad (32a)$$

$$\phi(\mathbf{x}, t) = -\frac{y}{\Lambda}, \quad (32b)$$

describing radial advection of a blob structure with an arbitrary initial radial distribution given by $\vartheta(x)$. The radial filament velocity is given by $1/\Lambda$, or in dimensional units by

$$\frac{V}{C_s} = \frac{2L_{\parallel} \rho_s^2}{R \ell^2}. \quad (33)$$

This velocity is inversely proportional to the square of the structure size, fundamentally different from the inertial blob velocity scaling in Eq. (25). However, there are several limitations on the validity of the blob solution (32), the most severe being the assumption of a sheath-connected SOL regime. The relevance of the above velocity scaling will be discussed further in Sec. V.

IV. NUMERICAL SIMULATIONS

Numerical solutions of the interchange model (14) have been obtained using a standard spectral method. Particular care has been taken such that the simulations are well converged with respect to the size of the simulation domain and the grid resolution. In this section, results are presented from a series of simulations using the symmetric blob structure in Eq. (18) as initial condition while there is initially no flow.

A. Rayleigh number variation

An isolated blob structure initially accelerates and move radially due to the formation of dipolar electrostatic potential and vorticity fields. An example of this is presented in Fig. 2, showing the two-dimensional distribution of the thermodynamic variable, the electric drift vorticity, the radial electric drift velocity, and the electrostatic potential for $\text{Ra} = 10^4$ and unit Prandtl number after one ideal interchange time. Note that only a small part of the full simulation domain is shown. The initial evolution is characterized by the formation of a front across which the thermodynamic variable varies sharply. The radial blob advection is evidently a result of the interchange motions associated with the vertical polarization of vorticity.

The front development is shown more clearly by the radial variation of the thermodynamic variable on the symmetry axis $y=0$, presented in Fig. 3(a). The leading front is followed by a trailing wake, while the amplitude decays with time due to collisional diffusion and stretching by the convective flow. The peak of the radial convective velocity, shown in Fig. 3(b), lags behind the front of the blob structure, resulting in a dispersive propagation. This enforces the

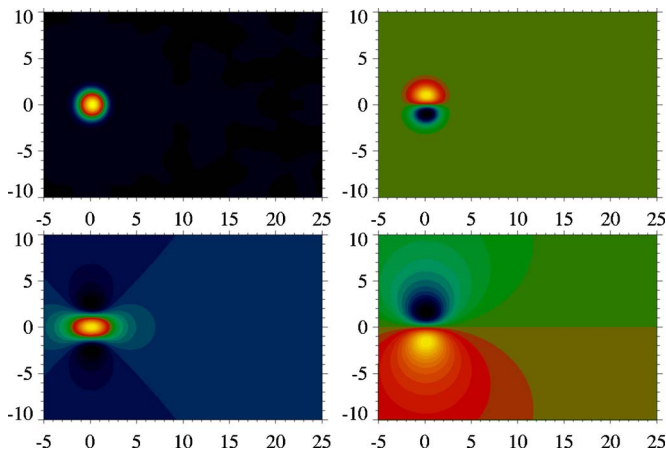


FIG. 2. (Color online) Spatial structure of the thermodynamic variable θ (top left panel), the vorticity Ω (top right panel), the radial velocity v_x (bottom left panel), and the electrostatic potential ϕ (bottom right panel) after one interchange time.

steepening of the leading edge of the blob structure, which thus locally resembles the dynamics of a shock front. The temporal variations obtained from probe recordings at various radial positions on the symmetry axis, shown in Fig. 4, are essentially the reverse of the structure in the spatial domain.

The late dynamical evolution of an initially symmetric blob structure for $Ra=10^4$ and $Pr=1$ is presented in Fig. 5.

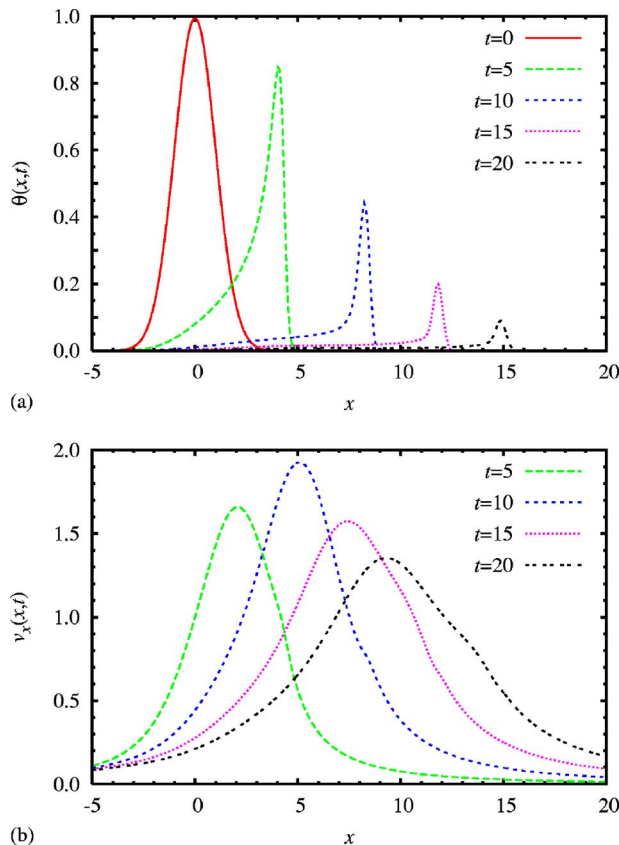


FIG. 3. (Color online) Radial variation of (a) the thermodynamic variable θ and (b) the radial electric drift v_x on the symmetry axis for $Ra=10^4$ and $Pr=1$.

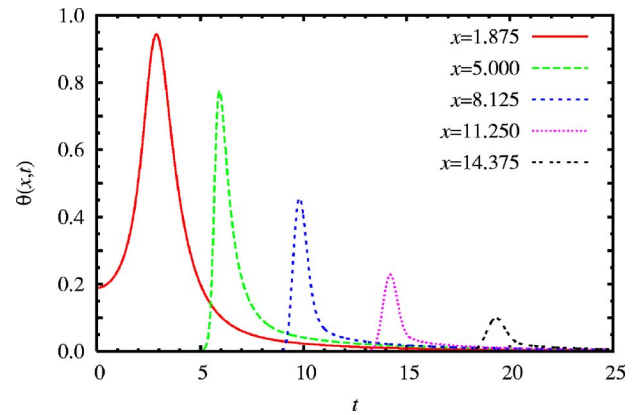


FIG. 4. (Color online) Evolution of the thermodynamic variable θ recorded on the symmetry axis at different radial positions for $Ra=10^4$ and $Pr=1$.

Here it is seen that the thermodynamic variable develops into the shape of a mushroom-like cap, a structure that is well known for scalar fields subject to interchange motions. Later on, the initially localized blob structure rolls up in two lobes. Due to stretching and collisional diffusion, the leading front eventually vanishes, leaving two disjoint entities each containing net vorticity of opposite polarity. The associated in-

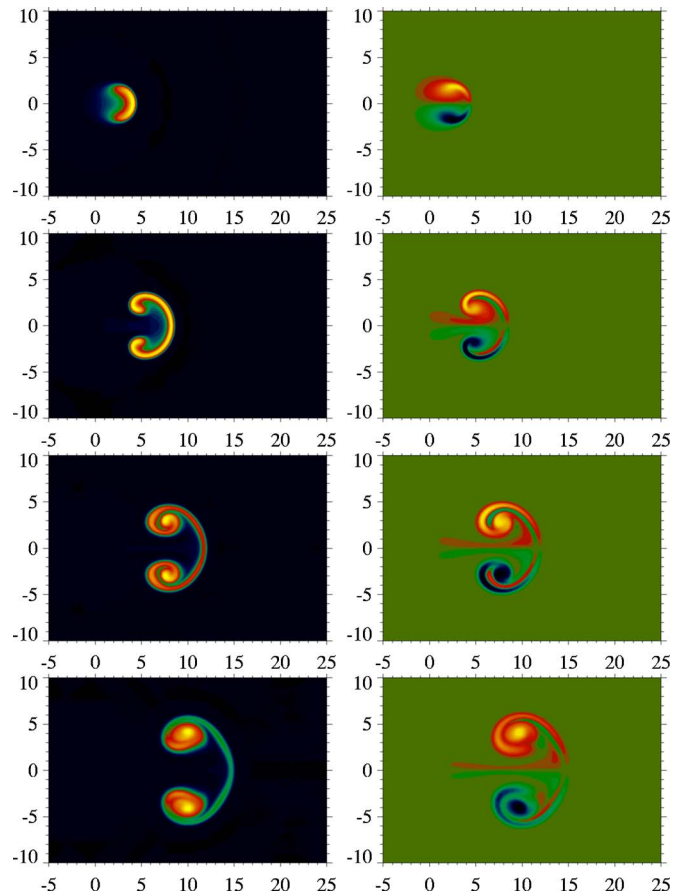


FIG. 5. (Color online) Evolution of an isolated blob structure for $Ra=10^4$ and $Pr=1$, showing the thermodynamic variable θ in the left column and the vorticity Ω in the right column at time $t=5$ in the top row and increments of five time units downwards.

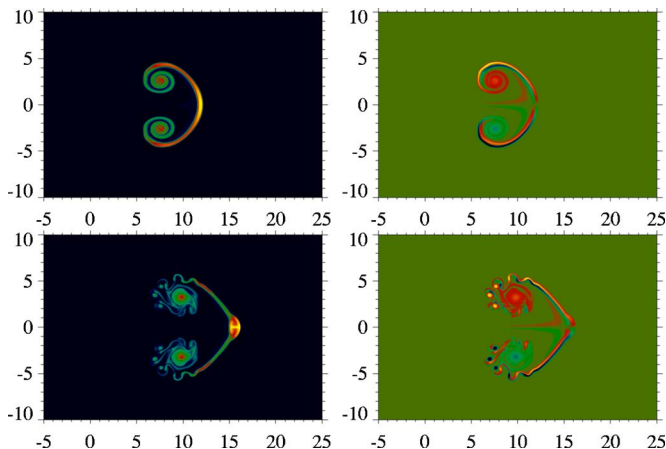


FIG. 6. (Color online) Evolution of an isolated blob structure for $Ra=10^6$ and $Pr=1$, showing the thermodynamic variable θ in the left column and the vorticity Ω in the right column at time $t=15$ in the top row and time $t=20$ in the bottom row.

ternal spin of these fragmented structures prevents further radial advection by a secondary polarization of vorticity, effectively bringing the radial motion to halt.

The early evolution of the initially symmetric blob structure seen in Fig. 5 is a general feature for large Rayleigh numbers. However, the details of the late evolution depend sensitively on the parameters. Another example for $Ra=10^6$ and $Pr=1$ is presented in Fig. 6, again showing the evolution of the thermodynamic variable and the electric drift vorticity. The strong vertical gradients in θ at the top and bottom spiral arms cause a secondary polarization of vorticity. This results in the formation of thin vorticity sheaths that are hydrodynamically unstable and cause the vorticity to roll up in an array of dipolar vortices. The result is efficient mixing and rapid dissipation due to the small spatial scales that develop. In the last frame of Fig. 6 we also observe that the leading front is itself unstable, generating a secondary plume structure. At larger Ra there is likely to occur a cascade of such higher-order instabilities, strongly enhancing mixing and dissipation of filamentary structures. The radial profile of the thermodynamic variable at various times is presented in Fig. 7 for $Ra=10^6$. It is interesting to note how the dynamical

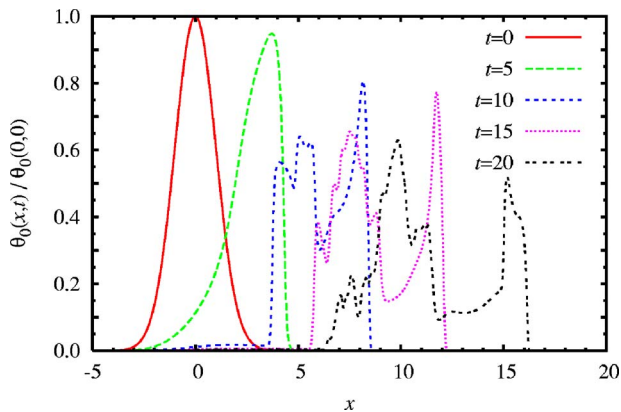


FIG. 7. (Color online) Radial profile of the thermodynamic variable θ for $Ra=10^6$ and $Pr=1$.

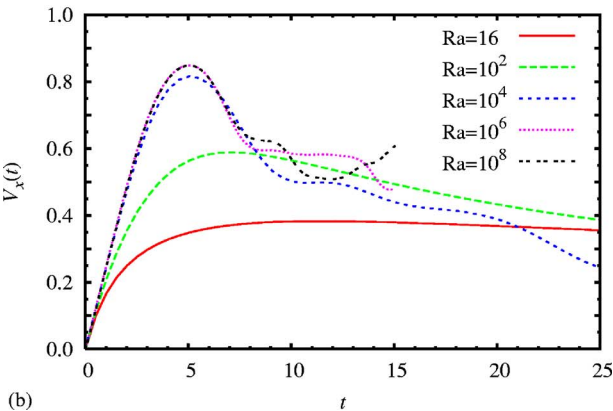
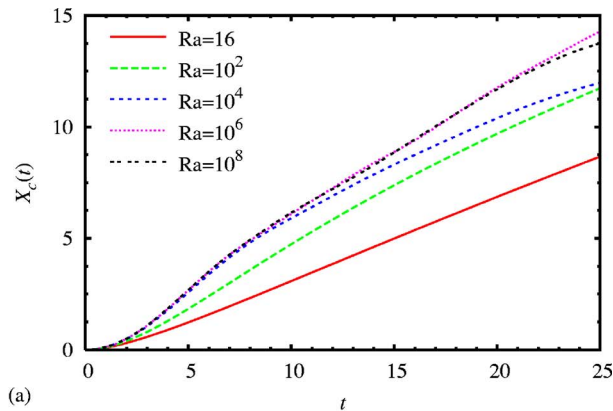


FIG. 8. (Color online) Evolution of the radial center of mass (a) position and (b) velocity for different Rayleigh numbers at $Pr=1$.

evolution leads to a rather complex waveform with several pronounced peaks even for an isolated plasma filament.

While the details of the late evolution at large Rayleigh numbers are highly sensitive to the specific values of the model parameters, the initial evolution is robust and leads to motion over a radial distance many times the initial size of the blob structure. This is clearly seen in Fig. 8(a), where we present the evolution of the radial center-of-mass coordinate for a large variation of the Rayleigh number. The corresponding radial center-of-mass velocity is presented in Fig. 8(b). For small Rayleigh numbers, the radial motion is slow but persists for a long period after the initial acceleration. This is because the structure maintains its initial blob-like shape during the radial motion. For larger Rayleigh numbers, the advection is much faster and there is a pronounced peak of the radial center-of-mass velocity. The deceleration at late times is associated with the blob dispersion seen in Figs. 5 and 6.

As remarked in connection with Figs. 3 and 4, the peak amplitude of the blob structure decays in time. In Fig. 9 we present the temporal evolution of the maximum amplitude of the thermodynamic variable for a large variation of the Rayleigh number. Since there is no vertical convective velocity component on the symmetry axis, the amplitude decay is due to collisional diffusion. This is verified by the blob amplitude evolution due to collisional diffusion alone, described by Eq. (19), which is represented by the thin lines in Fig. 9. Accordingly, the rate of decay of the peak blob amplitude decreases

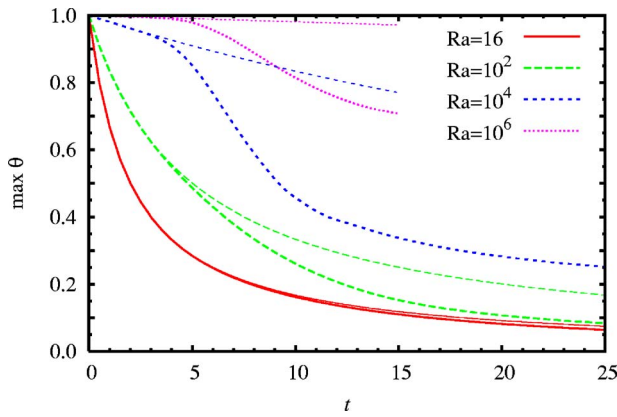


FIG. 9. (Color online) Evolution of the maximum blob amplitude for different Rayleigh numbers at $Pr=1$. The thin lines represent the amplitude decay due to diffusion alone, given by Eq. (19).

with increasing Rayleigh number, that is, with decreasing collisional diffusion. It should also be noted that the large-scale advection enhances the vertical gradients in θ close to the symmetry axis at the blob front and thus the rate of collisional diffusion and peak amplitude decay. This implies that the peak amplitude decay is effectively due to a combination of collisional diffusion and stretching by the convective motions.

Mixing of the blob structure is quantified by the dispersion tensor components defined in Sec. III B, or perhaps more clearly by the effective diffusivities whose evolution for a range of Rayleigh numbers is presented in Fig. 10. Note that the logarithmically scaled vertical axes show an estimate of the effective diffusivities relative to the collisional value κ . From this figure it is clear that after the transient acceleration, the blob structure disperses at a roughly constant rate with faster spreading in y than in x , the latter being due to the roll up seen in Figs. 5 and 6. For small Rayleigh numbers, or equivalently for large collisional diffusion κ , the effective diffusivities are close to the collisional values. With increasing Ra , the effective diffusivity supersedes by far that due to collisions.

In Fig. 11, we present the variation of the maximum radial center-of-mass velocity obtained from numerical simulations at unit Prandtl number, covering eight orders of magnitude variation in the Rayleigh number. As predicted by the theoretical considerations in Sec. III B, the maximum velocity becomes independent of collisional dissipation for sufficiently large Rayleigh numbers. The transition to this ideal regime occurs at $Ra \sim 10^4$, above which the maximum radial center-of-mass velocity remains constant at a value slightly less than unity. This corresponds to the inertial velocity scaling in the ideal limit given by Eq. (25). Note that the robust initial evolution for large Rayleigh numbers is also evident from Fig. 8, where the curves fall on top of each other up to about 10 ideal interchange time units. As seen in Fig. 8(a), the blob structure has by then traveled a radial distance more than five times its initial size. After the initial phase of acceleration, mixing and dispersion dominates the evolution, slowing down the radial motion.

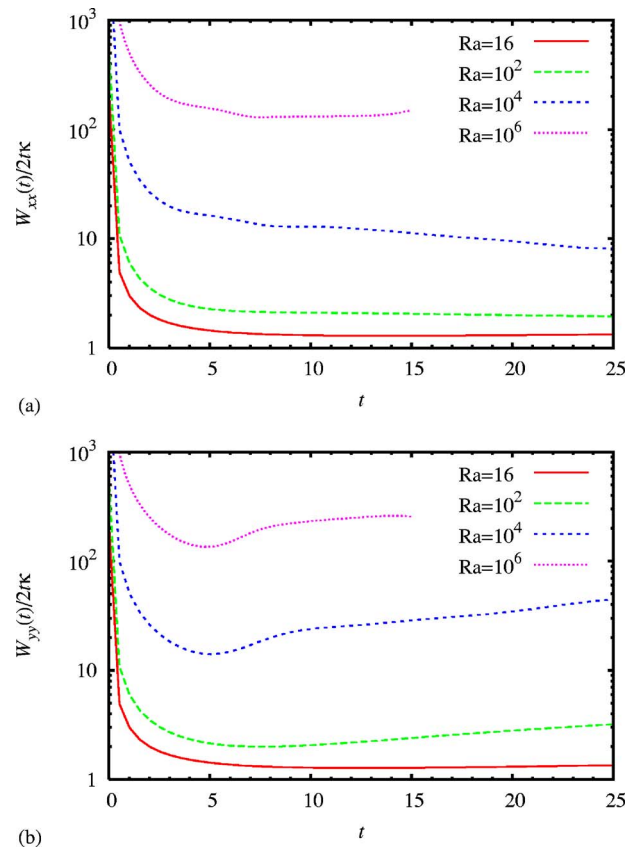


FIG. 10. (Color online) Evolution of the effective (a) radial and (b) poloidal diffusion coefficients for different Rayleigh numbers at $Pr=1$.

B. Prandtl number variation

In the previous section, we demonstrated the possibility for mixing and dispersion of blob structures. However, depending on the relative strength of viscosity and diffusion, the plasma filament can travel a large radial distance without significant changes in its spatial shape for relatively small Ra . One example is presented in Fig. 12 for $Ra=10^2$ and $Pr=4 \times 10^{-2}$. Due to strong collisional diffusion, the blob structure broadens while the polarization of vorticity makes it travel slowly outwards. The development of a steep front is again observed to take place, and the blob maintains its

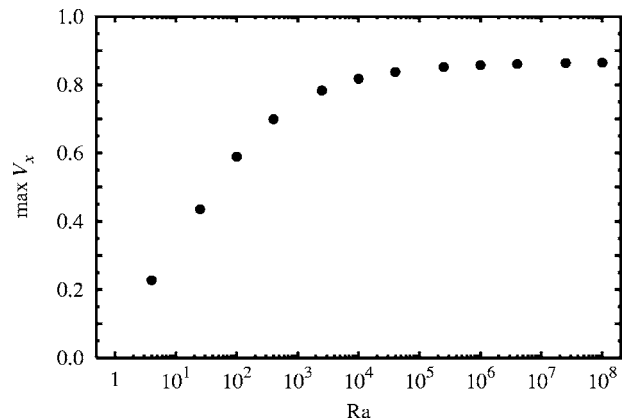


FIG. 11. Maximum radial center-of-mass velocity of an isolated blob structure as a function of the Rayleigh number for $Pr=1$.

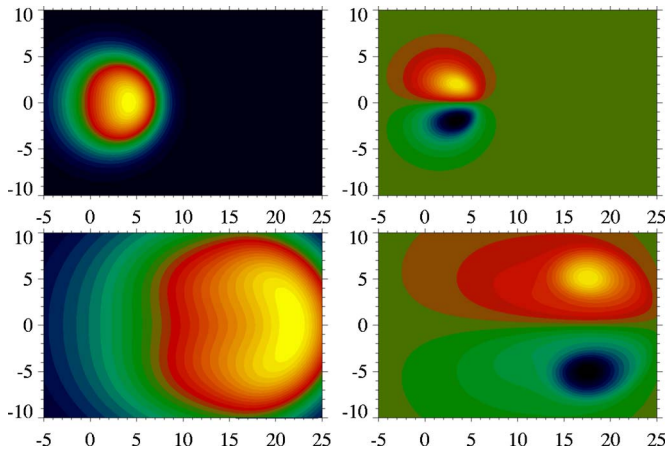


FIG. 12. (Color online) Evolution of an isolated blob structure for $Ra = 10^2$ and $Pr = 4 \times 10^{-2}$, showing the thermodynamic variable θ in the left column and the vorticity Ω in the right column at time $t=10$ in the top row and time $t=50$ in the bottom row.

shape while being advected a radial distance many times its initial size. Another example of a blob structure traveling a large radial distance without significant changes in its shape is presented in Fig. 13 for $Ra = 10^2$ and $Pr = 4 \times 10^2$, where viscous dissipation dominates over diffusion. In this case, the blob structure remains spatially localized with a length scale given by its initial size. For intermediate Pr and larger Ra , the blob structure is subject to strong dispersion like that seen in Fig. 5.

The temporal evolutions of the radial center-of-mass coordinate and velocity are presented in Fig. 14 for a wide range of Prandtl numbers at $Ra = 10^2$. This shows that the radial advection is relatively slow at small as well as large Prandtl numbers. Moreover, for large Pr the strong viscous dissipation leads to a very slow acceleration to the maximum radial center-of-mass velocity. For small Pr , the strong diffusion leads to radial advection at a nearly constant velocity after the initial acceleration. For intermediate Prandtl numbers, there is a fragmentation of the blob structure similar to

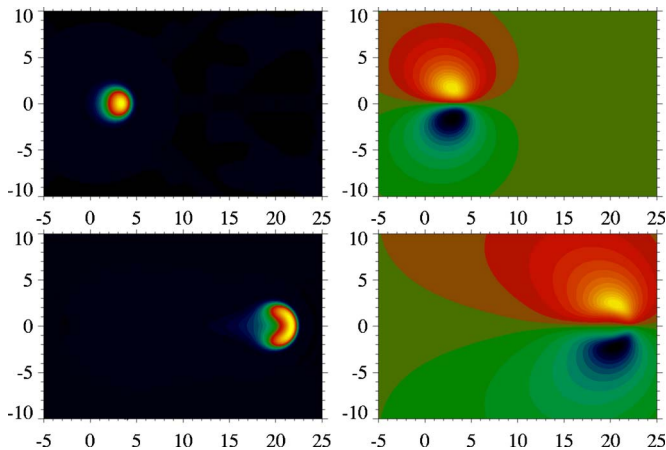


FIG. 13. (Color online) Evolution of an isolated blob structure for $Ra = 10^2$ and $Pr = 4 \times 10^2$, showing the thermodynamic variable θ in the left column and the vorticity Ω in the right column at time $t=10$ in the top row and time $t=50$ in the bottom row.

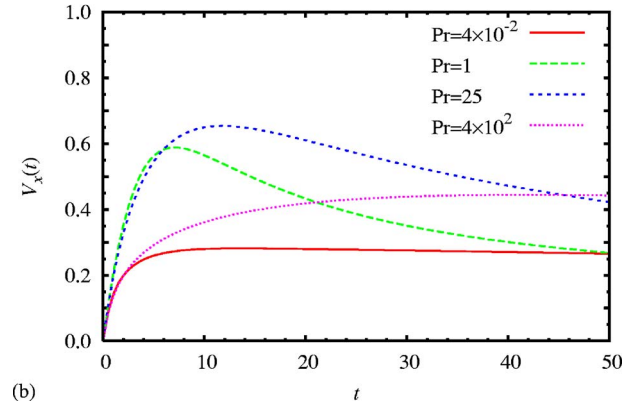
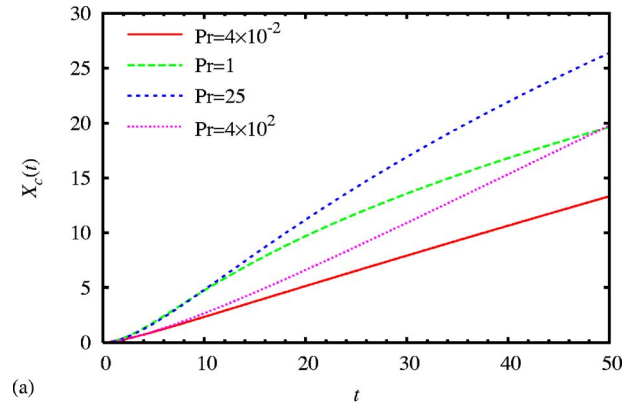


FIG. 14. (Color online) Evolution of the radial center of mass (a) position and (b) velocity for different Prandtl numbers at $Ra = 10^2$.

that seen in Fig. 5, but initially a much faster radial motion. The evolution of the maximum blob amplitude is presented in Fig. 15 for a range of Prandtl numbers. The amplitude decay is clearly caused by collisional diffusion and thus becomes slower with increasing Pr . For intermediate Prandtl numbers, the amplitude decay at late times is significantly faster than that described by diffusion alone. As discussed in the preceding section, this is due to the vertical stretching of the blob structure by the large-scale convective motions, enhancing the vertical gradient, and thus collisional diffusion in the vicinity of the symmetry axis.

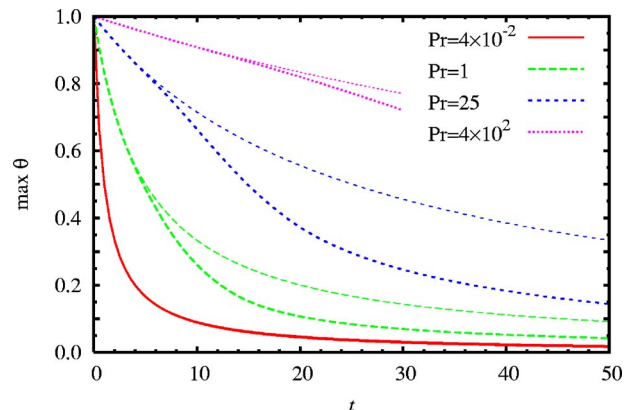


FIG. 15. (Color online) Temporal evolution of the maximum blob amplitude for different Prandtl numbers at $Ra = 10^2$. The thin lines represent the amplitude decay due to diffusion alone, given by Eq. (19).

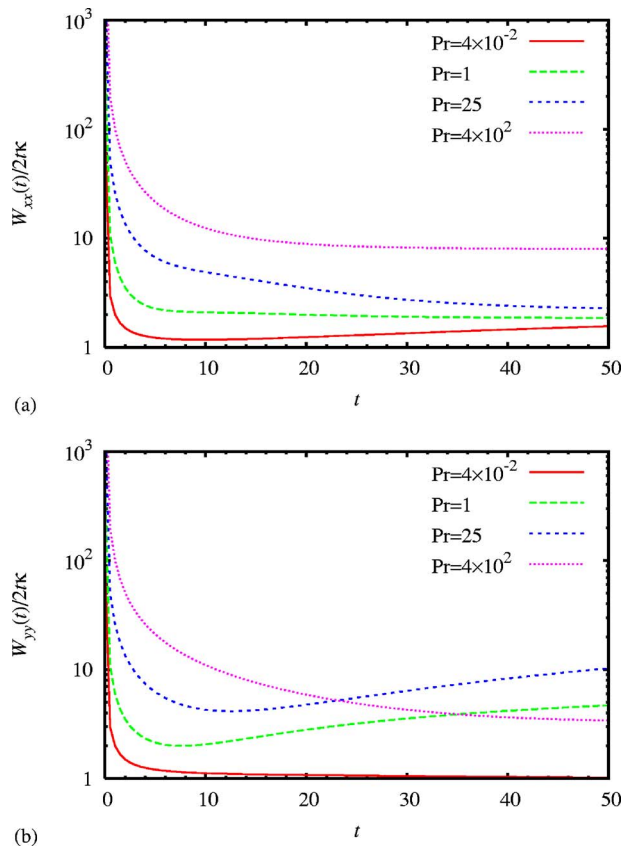


FIG. 16. (Color online) Evolution of the effective (a) radial and (b) poloidal diffusion coefficients for different Prandtl numbers at $Ra=10^2$.

The effective diffusivities due to dispersion of the blob structure are presented in Fig. 16. For the radial dispersion we see that the effective diffusivity becomes increasingly anomalous with increasing Prandtl number, which means decreasing collisional diffusion κ . For intermediate Prandtl numbers, strong vertical dispersion of the blob structure leads to a significant increase in the effective diffusivity D_y as seen in Fig. 16(b). However, for both large and small Prandtl numbers at $Ra=10^2$, the blob structure travels without significant distortions in its shape, resulting in the relatively small and temporally decreasing diffusivities seen in Fig. 16(b).

In Fig. 17, we present the variation of the maximum radial center-of-mass velocity with the Prandtl number for three different Rayleigh numbers. The radial velocity and thus the convective transport have a peak at an intermediate value of the Prandtl number. This may be understood from the fact that for small Prandtl numbers, the collisional diffusion is relatively strong and tends to oppose the radial advection, while the high viscosity for large Prandtl numbers evidently limits the flow amplitude. However, also the Prandtl number dependence becomes negligible with increasing Rayleigh number, consistent with the inertial velocity scaling in Eq. (25).

C. Sheath dissipation

The role of sheath dissipation has been strongly emphasized in many previous theories and numerical simulations of

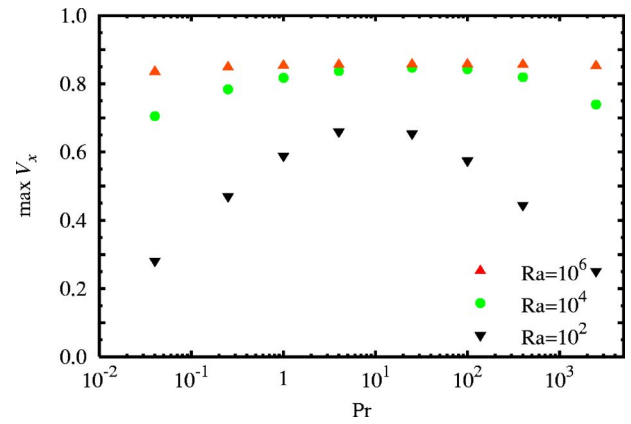


FIG. 17. Maximum radial center-of-mass velocity for an isolated blob structure as a function of the Prandtl number for three fixed Rayleigh numbers.

radial blob motion. The balance between this electric current channel and the interchange drive results in streamlines for the convective motions that are confined entirely within the localized blob structure. This should be contrasted to the large-scale flows associated with the inertial response seen in Fig. 2. In the following, we present results from a numerical investigation of the role of sheath dissipation for the radial motion of an isolated blob structure. The model equations (28) are solved for the same initial conditions as before, that is, the symmetric blob structure given by Eq. (18), while there is initially no flow.

In Fig. 18, we present the evolution of the thermodynamic variable and the electrostatic potential for $Ra=10^4$, $Pr=1$, and $\Lambda=1$. In this case, the initially symmetric blob structure develops a steep front and a long tail, while the dipolar electrostatic potential is entirely localized to the regions of vertical gradients in the thermodynamic variable. In addition to reducing the vertical dispersion and enhancing the radial dispersion of the blob structure, the sheath dissipation also leads to a much slower radial motion. For larger

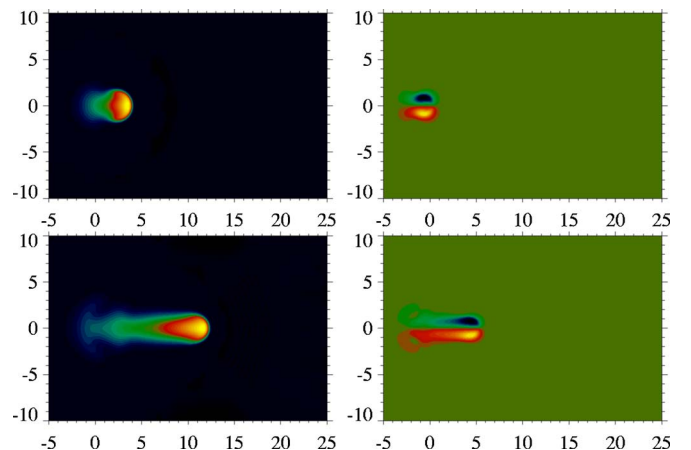


FIG. 18. (Color online) Evolution of an isolated blob structure for $Ra=10^4$, $Pr=1$, and $\Lambda=1$, showing the thermodynamic variable θ in the left column and the electrostatic potential ϕ in the right column at time $t=10$ in the top row and $t=50$ in the bottom row.

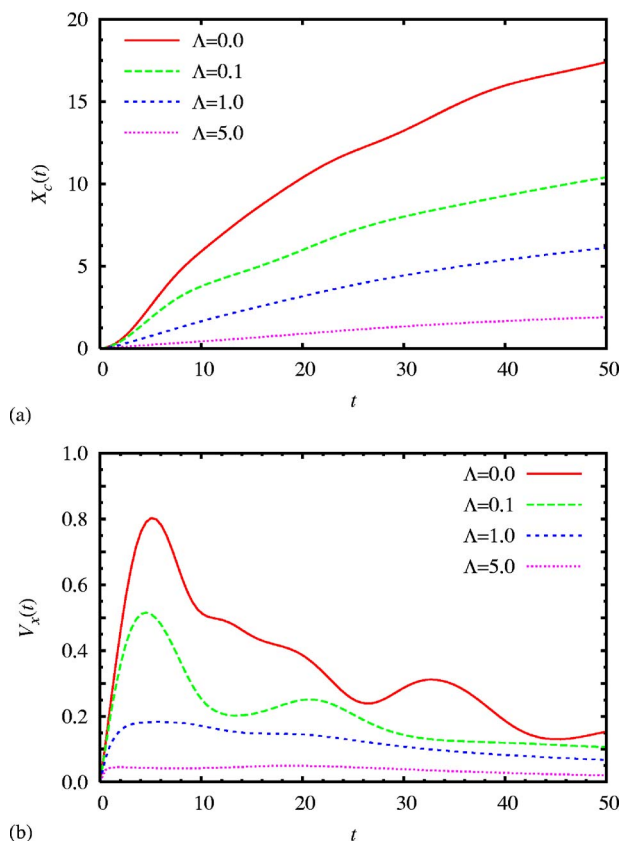


FIG. 19. Evolution of the radial center of mass (a) position and (b) velocity for different sheath dissipation coefficients at $Ra=10^4$ and $Pr=1$.

Rayleigh numbers, or smaller collisional dissipation, the blob structure is subject to instabilities, generating very small length scales.

The influence of sheath dissipation on radial blob motion is further revealed by the temporal evolutions of the radial center-of-mass coordinate and velocity, presented in Fig. 19 for $Ra=10^4$ and $Pr=1$ for various values of Λ . Here it is clearly seen that the advection velocity and thus the radial transport are strongly reduced with increasing sheath dissipation. This is in accordance with the dissipative effect of sheath currents and its preferential damping of large spatial length scales. In Fig. 20, we present the maximum radial blob velocity as function of the sheath dissipation parameter for three different Rayleigh numbers at unit Prandtl number. The maximum blob velocity decreases with increasing sheath dissipation for any given Ra . For large values of Ra and Λ , the structure develops thin vorticity sheets that are hydrodynamically unstable and lead to enhanced mixing and dissipation. The full line shown in Fig. 20 is the velocity scaling corresponding to the analytical blob solution described by Eq. (32). This clearly does not represent a good fit to any of the simulation results.

V. DISCUSSION

In this section, the results from the numerical simulations are discussed in relation to experimental measurements of filamentary structures at the boundary of magnetically

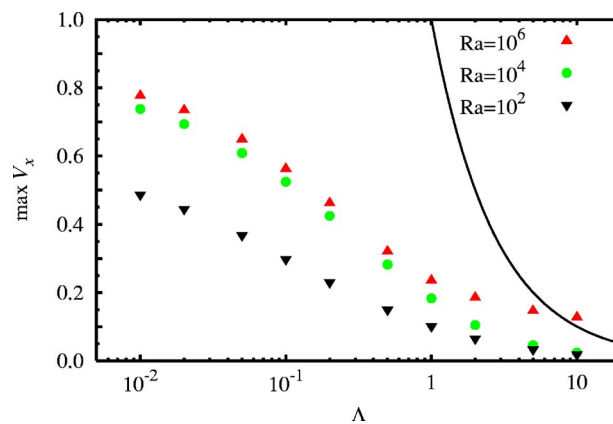


FIG. 20. Maximum radial center-of-mass velocity for an isolated blob structure as a function of the sheath dissipation parameter for three fixed Rayleigh numbers at unit Prandtl number. The full line shows the velocity scaling predicted by the analytical blob solution given in Eq. (32).

confined plasmas, comprising intermittent transport by blob-like structures in low confinement modes and ELM filament dynamics in high confinement modes.

A. SOL turbulence

In low confinement modes, the SOL plasma is generally found to exhibit large relative fluctuation levels. Moreover, the plasma fluctuations are strongly intermittent, with positively skewed and flattened single-point probability distribution functions. Conditional averaging of ion saturation current signals reveals a predominance of bursts in the time series with a steep front and a trailing wake.¹⁻¹³ These features are generally taken as a signature of radial structure motion, an interpretation that finds strong support by fast camera imaging of the edge plasma fluctuations.¹²⁻¹⁶ These structures are reported to have a spatial size perpendicular to the magnetic field of 0.5–2 cm and radial velocities of 1–10% of the acoustic speed in the SOL. Radial transport by localized structures due to interchange motions appears as an evident candidate mechanism to explain these experimental observations. In particular, a statistical ensemble of such filaments with varying sizes and amplitudes is most likely what underlies the broad particle density profiles, large relative fluctuation levels, and the strongly skewed and flattened single-point probability distributions.⁸²⁻⁸⁵

In order to relate the present results to these experimental observations, let us begin by considering the typical magnitude of the model parameters for a medium-sized tokamak plasma. Characteristic SOL parameters are taken to be

$$n \approx 10^{19} \text{ m}^{-3}, \quad T_e \approx 25 \text{ eV}, \quad T_i \approx 25 \text{ eV}, \quad (34a)$$

$$R \approx 1 \text{ m}, \quad B \approx 1 \text{ T}, \quad q \approx 3, \quad (34b)$$

where q is the safety factor in the vicinity of the separatrix and the parallel connection length L_{\parallel} in the SOL may be approximated by $\pi q R \approx 10 \text{ m}$. For the blob structure we anticipate a size and relative amplitude of

$$\ell \approx 10^{-2} \text{ m}, \quad \frac{\Delta\theta}{\Theta} \approx 0.5, \quad (35)$$

which are typical values reported from experimental measurements. This yields the following dimensional parameters for the interchange dynamics:

$$\rho_s \approx 10^{-3} \text{ m}, \quad C_s \approx 5 \times 10^4 \text{ m s}^{-1}, \quad (36a)$$

$$g \approx 5 \times 10^9 \text{ m s}^{-2}, \quad \gamma \approx 5 \times 10^5 \text{ s}^{-1}. \quad (36b)$$

According to these values, the ideal blob velocity, given by Eq. (25), relative to the acoustic speed becomes 0.1, or 5 km s^{-1} in dimensional units. While such a large velocity has been reported from some experiments, we read from Fig. 8 that the average velocity over ten interchange times is smaller by roughly a factor 2 in the ideal limit, in good agreement with experiments. Additionally, these results do not take into account transport along the field lines. We further note that the interchange time scale, $1/\gamma \approx 2 \mu\text{s}$, compares favorably with the correlation time derived from experimental probe measurements. The figures in the preceding section can thus be read by identifying unity time with $2 \mu\text{s}$, unit length with 1 cm, and unit velocity with 5 km s^{-1} .

In order to estimate collisional diffusion and viscosity parameters, we take into account neoclassical corrections.⁸⁶ Based on particle diffusivity, the Rayleigh and Prandtl numbers for the above-stated plasma parameters become $\text{Ra} \approx 5 \times 10^5$ and $\text{Pr} \approx 20$, which in the absence of parallel motions is well into the ideal regime according to Figs. 11 and 17. We conclude that if two-dimensional interchange motions govern the collective dynamics for these plasma parameters, an isolated blob structure would accelerate, develop a steep front and a trailing wake, move a radial distance many times its initial size, and eventually decelerate due to dispersion in the drift plane perpendicular to the magnetic field. In practice, the blob structure would have traveled far into the limiter or wall shadow, which is typically separated from the magnetic separatrix by only a few centimeters when mapped to the outer midplane. Radial transport by plasma filaments driven by interchange motions thus appears as the salient mechanism underlying the so-called main chamber recycling regime, a situation in which the plasma recycles by interaction with the main chamber walls rather than in the divertor region.^{21–26}

With a parallel connection length in the SOL of roughly 10 m, the dimensionless sheath dissipation parameter $\Lambda \approx 2$. Based on the results presented in Sec. IV C, this would in principle strongly influence the blob dynamics. In particular, it would reduce the maximum radial blob velocity by a factor of 4. For $\text{Ra} = 10^6$, $\text{Pr} = 1$, and $\Lambda = 2$ this yields a nearly constant average velocity of 0.15 up to 30 interchange time units. For a structure size of 1 cm, this velocity corresponds to 0.015 in units of C_s , or 750 m s^{-1} in dimensional units, which is also comparable with the typical values reported from experimental estimates. However, as has been discussed in Sec. II C, some caution must be taken when applying the sheath dissipation term in order to describe the effect of parallel currents in the region of open field lines. Ballooning in the turbulent transport and finite collisionality would

effectively prevent a sheath-limited regime. For the above given parameters, the particle collisionality in the SOL plasma $\nu_e^* = L_{\parallel}/\lambda_{ei} \approx 20$, where λ_{ei} is the electron-ion mean free path. Magnetic equilibrium reconstruction often yields a substantially larger connection length, and hence an even stronger plasma collisionality and a correspondingly smaller sheath dissipation coefficient. The effect of sheath currents may also be limited by the competition between parallel and perpendicular transport. The plasma transport time scales in these two directions are given by L_{\parallel}/C_s and ℓ/V , respectively, where V is the radial blob velocity. A filamentary structure would thus travel a radial distance of the order of the structure size before one parallel transit time provided $V/C_s > \ell/L_{\parallel}$. Since ℓ/L_{\parallel} is typically of the order 10^{-3} , this is a fairly weak restriction on the radial velocity of plasma filaments and is well within the range of values reported from experimental measurements. While only a complete description of the parallel dynamics can resolve this important issue, the radial motion is certainly driven by the collective interchange dynamics. It is thus reassuring that the results presented here compare favorably with experimental measurements.

B. ELM filaments

In unstable high confinement modes, the edge transport barrier is quasiperiodically destroyed by what are known as edge localized modes. These relaxations of the edge plasma density and temperature profiles involve the formation of 10–20 localized plasma filaments that originate on the low-field side of the tokamak with particle densities and temperatures characteristic of the pedestal plasma. In the SOL region, the filaments experience strong parallel losses of particles and heat to the divertor targets. Yet they can deposit a significant fraction of their initial energy onto the main vessel wall. Radial ELM filament velocities in the SOL are typically reported to be in the range of $0.5\text{--}10 \text{ km s}^{-1}$ while their size in the plane perpendicular to the magnetic field is in the range of 1–5 cm. Probe measurements have further revealed that there is substantial fine-scale structure associated with ELM filaments in the SOL, comprising pulses with a duration of 10–50 μs and varying amplitude and repetition rates.^{28–43}

There are presently two leading candidate theories of ELM filament dynamics. The first is based on the explosive ballooning of pedestal flux tubes described by ideal magnetohydrodynamics.^{87–89} The second is based on the sheath-dissipative blob solution given in Eq. (32). Unfortunately, both of these theories suffer from significant shortcomings when compared to experimental data, thus motivating the continued search for a satisfactory model.^{42,43} In the following, we argue that electrostatic interchange motions described in this work offer significant improvements in explaining the observed ELM filament dynamics. In particular, this complies with the experimental measurements of ballooning, transport-driven parallel flows, fine scales of the ELM substructure, and the radial filament velocity.

As in the previous section, we begin by considering the typical magnitude of the model parameters, this time for a

large tokamak plasma from which most of the observational data on ELM filaments are reported. Characteristic SOL parameters are taken to be

$$n \approx 10^{19} \text{ m}^{-3}, \quad T_e \approx 50 \text{ eV}, \quad T_i \approx 100 \text{ eV}, \quad (37a)$$

$$R \approx 2 \text{ m}, \quad B \approx 2 \text{ T}, \quad q \approx 3, \quad (37b)$$

while the ELM filament size and relative amplitude are taken in line with typical values reported from experimental measurements,

$$\ell \approx 2 \times 10^{-2} \text{ m}, \quad \frac{\Delta\theta}{\Theta} \approx 5. \quad (38)$$

The ELM filament represents a relative perturbation to the SOL background parameters larger by an order of magnitude compared to blob structures observed in low confinement modes. This strong nonlinearity poses several problems to the reduced model equations applied in this work. First, a fully nonlinear treatment should be made for the vorticity equation, thus implying the logarithmic form of the particle density interchange drive given in Eq. (31). For a finite background plasma density, this introduces $\Delta\theta/\Theta$ as an additional free parameter in the problem. Moreover, separate model equations for both the plasma density and heat should be included. And finally, variations of the plasma parameters should be taken into account for the collisional diffusion and viscosity. Indeed, while the background plasma as given by the parameters in Eq. (37) is collisional with $\nu_e^* \approx 10$, application of the peak ELM filament parameters results in $\nu_e^* \approx 0.1$ for $L_{\parallel} = 20 \text{ m}$. The collisionless conditions of such hot filament structures imply that the sheath-connected regime is likely to be more relevant than in the case of low confinement modes.

It is thus instructive to examine the predictions of the simple two-field interchange model, keeping in mind the limitations of these equations when applied to the ELM filament problem. The relevant dimensional parameters are evaluated as

$$\rho_s \approx 10^{-3} \text{ m}, \quad C_s \approx 8 \times 10^4 \text{ m s}^{-1}, \quad (39a)$$

$$g \approx 7 \times 10^9 \text{ m s}^{-2}, \quad \gamma \approx 10^6 \text{ s}^{-1}, \quad (39b)$$

such that the ideal blob velocity now becomes 0.3, or approximately 25 km s^{-1} in dimensional units. Note that according to Fig. 11, the average center-of-mass velocity up to ten interchange times is smaller by roughly a factor of 2 in the absence of parallel motions. The Rayleigh and Prandtl numbers, again based on particle diffusivity, are found to be $\text{Ra} \approx 2 \times 10^9$ and $\text{Pr} \approx 10$. Finally, the dimensionless sheath dissipation parameter is evaluated as $\Lambda \approx 3$. With these default values, all the figures presented in this work should be interpreted by identifying unity time with $1 \mu\text{s}$, unit length with 2 cm , and unit velocity with 25 km s^{-1} . Note that if the Rayleigh number is estimated with respect to the peak amplitude particle density, it will be reduced to $\text{Ra} \approx 10^8$, which is still well into the ideal regime according to Figs. 11 and 17.

The maximum radial center-of-mass velocity in the presence of sheath dissipation, presented in Fig. 20, is compat-

ible with the experimentally estimated average filament velocity of the order of a few kilometers per second. From Fig. 20 we see that sheath dissipation reduces the maximum radial center-of-mass velocity by a factor of 5 to roughly 5 km s^{-1} in dimensional units, in agreement with experimental measurements. In a sheath-detached blob regime, we would expect the parallel plasma motion to similarly reduce the blob amplitude and thereby the radial velocity. Moreover, the complex waveform due to dispersion of isolated structures, such as that seen in Fig. 7, resembles experimental probe measurements. The probe signals may also be influenced by rotation of an array of toroidally and poloidally localized filaments erupted from the plasma edge. We conclude that the radial velocities and fine structure of ELM filaments observed in the SOL are consistent with the dynamical evolution governed by electrostatic interchange motions.

A remark is finally given to the scaling of the filament velocity with its amplitude and size perpendicular to the magnetic field. The inertial velocity scaling given in Eq. (25) predicts a radial filament velocity increasing with the filament size and amplitude, which should be contrasted to the sheath-dissipative velocity scaling given in Eq. (33). Probe measurements in the SOL have in fact indicated that the effective ELM filament velocity increases with the radial gradient of the structure itself, and thus with the amplitude of the filament.^{29,36} Such a size dependence of the filament velocity is also indicated by the observations of larger heat deposition on limiters and main chamber walls for large ELM events.⁹⁰ Further investigations are clearly required in order to resolve this crucial issue.

VI. CONCLUSIONS

In this contribution, the dynamics and transport properties of isolated plasma filaments due to interchange motions have been analyzed in detail. An initially localized blob-like structure accelerates radially outwards, develops a steep front and a trailing wake, and travels a radial distance many times its initial size. This motion results from a large-scale convective flow caused by the inertial response to magnetic guiding center drifts within the blob structure. For weak collisional dissipation and parallel losses, there is an inertial scaling with the velocity increasing as the acoustic speed times the square root of the structure size relative to the magnetic-field radius of curvature. Numerical simulations reveal that this velocity appears as a transient maximum value, preceded by a phase of acceleration and followed by dispersion and hence deceleration of the blob structure. The rich dynamical evolution is consistent with experimental measurements of transient transport events in the plasma boundary region.

The radial structure velocity, temporal scales, and dynamical evolution with a steep front and a trailing wake compare favorably with recent experimental measurements and fast camera imaging of turbulence in the boundary region of magnetically confined plasmas.¹⁻¹⁶ Moreover, the blob dynamics seen in these simulations resembles that observed in recent two-dimensional turbulence simulations of intermittent transport in the SOL region,⁸²⁻⁸⁵ including the

dipolar shape of the electrostatic potential and the electric drift vorticity that is associated with the blob structure. It should be noted that such a dipolar electric potential associated with blob structures has recently been measured experimentally,¹³ after first being predicted theoretically.⁶⁶ These results strongly indicate that interchange dynamics due to the nonuniform magnetic field is the mechanism that underlies radial motion of filamentary structures through the SOL of plasmas confined by a strong toroidal magnetic field.

In SOL plasmas, parallel transport along open magnetic-field lines will compete with radial transport due to interchange motions. In a sheath-connected regime, the effect of parallel electric currents can be approximated by a zero-dimensional sheath dissipation term. Most previous theories of radial structure motion have relied on this effective sheath dissipation. The simulations presented here reveal that sheath dissipation strongly reduces the radial velocity of blob structures. Application of the sheath dissipation term is likely to be relevant for the hot plasma filaments following ELM activity in high confinement modes. Results from numerical simulations are in good agreement with experimental measurements of the radial velocity and dynamical evolution of such structures. However, for sheath-detached filament structures, acoustic streaming along the field lines is more likely to limit the radial motion.^{82–85}

In summary, it is found that the dynamical evolution of isolated plasma filaments governed by interchange motions is consistent with a vast range of experimental measurements in both low and high confinement modes. These include a rich dynamical evolution comprising a rapid initial acceleration, development of a steep front and a trailing wake, fast radial motion over a distance many times the initial blob size, and eventually dispersion and deceleration of the filamentary structure. In low confinement mode operation, interchange driven radial structure motion thus appears as the salient mechanism underlying the experimentally observed broad plasma profiles, large relative fluctuation levels, asymmetric conditional waveforms, and positively skewed and flattened probability distribution functions. This again is most likely what causes the plasma to recycle on the main chamber walls rather than in the divertor region as intended.^{21–26} Electrostatic interchange motions also seems to be a serious candidate mechanism to describe the dynamics of and radial transport by ELM filaments. Further discussions of this latter topic will be presented in a separate contribution.⁴³

ACKNOWLEDGMENTS

Discussions with J. Egedal, V. Naulin, A. H. Nielsen, R. A. Pitts, J. J. Rasmussen, and S. J. Zweben are gratefully acknowledged.

O.E.G. was supported financially by the Research Council of Norway and the Danish Agency for Science, Technology and Innovation.

¹E. Sánchez, C. Hidalgo, D. López-Bruna *et al.*, Phys. Plasmas **7**, 1408 (2000).

²J. A. Boedo, D. Rudakov, R. Moyer *et al.*, Phys. Plasmas **8**, 4826 (2001).

³G. Y. Antar, S. I. Krasheninnikov, P. Devynck *et al.*, Phys. Rev. Lett. **87**, 065001 (2001).

⁴G. Y. Antar, P. Devynck, X. Garbet, and S. C. Luckhardt, Phys. Plasmas **8**, 1612 (2001).

⁵J. A. Boedo, D. L. Rudakov, R. A. Moyer *et al.*, Phys. Plasmas **10**, 1670 (2003).

⁶G. Y. Antar, G. Counsell, Y. Yu, B. Labombard, and P. Devynck, Phys. Plasmas **10**, 419 (2003).

⁷G. S. Kirnev, V. P. Budaev, S. A. Grashin, E. V. Gerasimov, and L. N. Khimchenko, Plasma Phys. Controlled Fusion **46**, 621 (2004).

⁸J. P. Graves, J. Horacek, R. A. Pitts, and K. I. Hopcraft, Plasma Phys. Controlled Fusion **47**, L1 (2005).

⁹J. Horacek, R. A. Pitts, and J. P. Graves, Czech. J. Phys. **55**, 271 (2005).

¹⁰G. Y. Antar, G. Counsell, and J.-W. Ahn, Phys. Plasmas **12**, 082503 (2005).

¹¹Y. H. Xu, S. Jachmich, R. R. Weynants, and the TEXTOR Team, Plasma Phys. Controlled Fusion **47**, 1841 (2005).

¹²J. L. Terry, N. P. Basse, I. Cziegler *et al.*, Nucl. Fusion **45**, 1321 (2005).

¹³O. Grulke, J. L. Terry, B. LaBombard, and S. J. Zweben, Phys. Plasmas **13**, 012306 (2006).

¹⁴S. J. Zweben, D. P. Stotler, J. L. Terry *et al.*, Phys. Plasmas **9**, 1981 (2002).

¹⁵S. J. Zweben, R. J. Maqueda, D. P. Stotler *et al.*, Nucl. Fusion **44**, 134 (2004).

¹⁶J. L. Terry, S. J. Zweben, K. Hallatschek *et al.*, Phys. Plasmas **10**, 1739 (2003).

¹⁷S. K. Erements, R. A. Pitts, W. Fundamenski, J. P. Gunn, and G. F. Matthews, Plasma Phys. Controlled Fusion **46**, 1757 (2004).

¹⁸N. Smick, B. LaBombard, and C. S. Pitcher, J. Nucl. Mater. **337–339**, 281 (2005).

¹⁹B. LaBombard, J. E. Rice, A. E. Hubbard *et al.*, Nucl. Fusion **44**, 1047 (2004).

²⁰G. S. Kirnev, V. P. Budaev, S. A. Grashin, L. N. Khimchenko, and D. V. Sarytchev, Nucl. Fusion **45**, 459 (2005).

²¹M. V. Umansky, S. I. Krasheninnikov, B. LaBombard, and J. L. Terry, Nucl. Fusion **40**, 2041 (2000).

²²B. LaBombard, M. V. Umansky, R. L. Boivin *et al.*, Nucl. Fusion **40**, 2041 (2000).

²³B. LaBombard, R. L. Boivin, M. Greenwald *et al.*, Phys. Plasmas **8**, 2107 (2001).

²⁴B. Lipschultz, B. LaBombard, C. S. Pitcher, and R. Boivin, Plasma Phys. Controlled Fusion **44**, 733 (2002).

²⁵D. G. Whyte, B. L. Lipschultz, P. C. Stangeby *et al.*, Plasma Phys. Controlled Fusion **45**, 1589 (2005).

²⁶D. L. Rudakov, J. A. Boedo, R. A. Moyer *et al.*, Plasma Phys. Controlled Fusion **45**, 1589 (2005).

²⁷R. A. Pitts, J. P. Coad, D. P. Coster *et al.*, Plasma Phys. Controlled Fusion **47**, B303 (2005).

²⁸D. L. Rudakov, J. A. Boedo, R. A. Moyer *et al.*, Plasma Phys. Controlled Fusion **44**, 717 (2002).

²⁹B. Gonçalves, C. Hidalgo, M. A. Pedrosa *et al.*, Plasma Phys. Controlled Fusion **45**, 1627 (2003).

³⁰W. Fundamenski, W. Sailer, and JET EFDA contributors, Nucl. Fusion **46**, 233 (2004).

³¹A. Kirk, G. F. Counsell, H. R. Wilson *et al.*, Plasma Phys. Controlled Fusion **46**, 551 (2004).

³²A. Kirk, H. R. Wilson, G. F. Counsell *et al.*, Phys. Rev. Lett. **92**, 245002 (2004).

³³A. Kirk, T. Eich, A. Herrmann *et al.*, Plasma Phys. Controlled Fusion **47**, 995 (2005).

³⁴M. Endler, I. García-Cortés, C. Hidalgo, G. F. Matthews, ASDEX Team, and JET Team, Plasma Phys. Controlled Fusion **47**, 219 (2005).

³⁵T. Eich, A. Herrmann, J. Neuhauser *et al.*, Plasma Phys. Controlled Fusion **47**, 815 (2005).

³⁶C. Silva, B. Gonçalves, C. Hidalgo *et al.*, J. Nucl. Mater. **337–339**, 722 (2005).

³⁷J. A. Boedo, D. L. Rudakov, E. Hollmann *et al.*, Phys. Plasmas **12**, 072516 (2005).

³⁸D. L. Rudakov, J. A. Boedo, R. A. Moyer *et al.*, Nucl. Fusion **45**, 1589 (2005).

³⁹R. A. Pitts, W. Fundamenski, S. K. Erements *et al.*, Nucl. Fusion **46**, 82 (2006).

⁴⁰W. Fundamenski, R. A. Pitts, and JET EFDA contributors, Plasma Phys. Controlled Fusion **48**, 109 (2006).

- ⁴¹A. Kirk, B. Koch, R. Scannell *et al.*, Phys. Rev. Lett. **96**, 185001 (2006).
- ⁴²A. W. Leonard, N. Asakura, J. A. Boedo *et al.*, Plasma Phys. Controlled Fusion **48**, A149 (2006).
- ⁴³W. Fundamenski, V. Naulin, T. Neukirch *et al.*, "On the relationship between ELMs and solar flares" Plasma Phys. Controlled Fusion (submitted for publication).
- ⁴⁴A. A. Townsend, J. Fluid Mech. **5**, 209 (1959).
- ⁴⁵T. Y. Chu and R. J. Goldstein, J. Fluid Mech. **60**, 141 (1973).
- ⁴⁶G. Zocchi, E. Moses, and A. Libchaber, Physica A **166**, 387 (1990).
- ⁴⁷E. Moses, G. Zocchi, and A. Libchaber, J. Fluid Mech. **251**, 581 (1993).
- ⁴⁸A. Belmonte and A. Libchaber, Phys. Rev. E **53**, 4893 (1996).
- ⁴⁹B. G. Fejer and M. C. Kelly, Rev. Geophys. Space Sci. **18**, 401 (1980).
- ⁵⁰S. L. Ossakow, J. Atmos. Terr. Phys. **43**, 437 (1981).
- ⁵¹M. C. Kelley, J. Atmos. Terr. Phys. **47**, 745 (1985).
- ⁵²D. L. Hysell, J. Atmos. Sol.-Terr. Phys. **62**, 1037 (2000).
- ⁵³G. Veronis, Astrophys. J. **137**, 641 (1963).
- ⁵⁴S. Musman, J. Fluid Mech. **31**, 343 (1968).
- ⁵⁵D. R. Moore and N. O. Weiss, J. Fluid Mech. **61**, 553 (1973).
- ⁵⁶S. I. Krasheninnikov, A. I. Smolyakov, G. Yu, and T. K. Soboleva, Czech. J. Phys. **55**, 307 (2005).
- ⁵⁷S. I. Krasheninnikov, Phys. Lett. A **283**, 368 (2001).
- ⁵⁸D. A. D'Ippolito, J. R. Myra, and S. I. Krasheninnikov, Phys. Plasmas **9**, 222 (2002).
- ⁵⁹S. I. Krasheninnikov, D. Ryutov, and G. Yu, J. Plasma Fusion Res. **6**, 139 (2004).
- ⁶⁰D. A. D'Ippolito and J. R. Myra, Phys. Plasmas **10**, 4029 (2003).
- ⁶¹D. A. D'Ippolito, J. R. Myra, S. I. Krasheninnikov, G. Q. Yu, and A. Yu. Pigarov, Contrib. Plasma Phys. **44**, 205 (2004).
- ⁶²A. Y. Aydemir, Phys. Plasmas **12**, 062503 (2005).
- ⁶³G. Q. Yu and S. I. Krasheninnikov, Phys. Plasmas **10**, 4413 (2003).
- ⁶⁴J. R. Myra, D. A. D'Ippolito, S. I. Krasheninnikov, and G. Q. Yu, Phys. Plasmas **11**, 4267 (2004).
- ⁶⁵D. A. D'Ippolito, J. R. Myra, D. A. Russell, and G. Q. Yu, Phys. Plasmas **11**, 4603 (2004).
- ⁶⁶N. Bian, J.-V. Paulsen, S. Benkadda, and O. E. Garcia, Phys. Plasmas **10**, 671 (2003).
- ⁶⁷O. E. Garcia, N. H. Bian, V. Naulin, A. H. Nielsen, and J. J. Rasmussen, Phys. Plasmas **12**, 090701 (2005).
- ⁶⁸R. D. Hazeltine and J. D. Meiss, Phys. Rep. **121**, 1 (1985).
- ⁶⁹O. E. Garcia, Eur. J. Phys. **24**, 331 (2001).
- ⁷⁰H. R. Strauss, Phys. Fluids **19**, 134 (1976).
- ⁷¹J. F. Drake and T. M. Antonsen, Jr., Phys. Fluids **27**, 898 (1983).
- ⁷²M. Yagi and W. Horton, Phys. Plasmas **1**, 2135 (1994).
- ⁷³B. Scott, Phys. Plasmas **10**, 963 (2003).
- ⁷⁴H. Sugama and W. Horton, Phys. Plasmas **1**, 345 (1994).
- ⁷⁵O. Pogutse, W. Kerner, V. Gribkov, S. Bazdenkov, and M. Osipenko, Plasma Phys. Controlled Fusion **36**, 1963 (1994).
- ⁷⁶P. Beyer and K. H. Spatschek, Phys. Plasmas **3**, 995 (1996).
- ⁷⁷O. E. Garcia, J. Plasma Phys. **65**, 81 (2001).
- ⁷⁸O. E. Garcia, N. H. Bian, J.-V. Paulsen, S. Benkadda, and K. Rypdal, Plasma Phys. Controlled Fusion **45**, 919 (2003).
- ⁷⁹O. E. Garcia and N. H. Bian, Phys. Rev. E **68**, 047301 (2003).
- ⁸⁰N. H. Bian and O. E. Garcia, Phys. Plasmas **12**, 042307 (2005).
- ⁸¹O. E. Garcia, N. H. Bian, V. Naulin, A. H. Nielsen, and J. J. Rasmussen, Phys. Scr., T **T122**, 104 (2006).
- ⁸²O. E. Garcia, V. Naulin, A. H. Nielsen, and J. J. Rasmussen, Phys. Rev. Lett. **92**, 165003 (2004).
- ⁸³O. E. Garcia, V. Naulin, A. H. Nielsen, and J. J. Rasmussen, Phys. Plasmas **12**, 062309 (2005).
- ⁸⁴O. E. Garcia, V. Naulin, A. H. Nielsen, and J. J. Rasmussen, Phys. Scr., T **T122**, 89 (2006).
- ⁸⁵O. E. Garcia, J. Horacek, R. A. Pitts, A. H. Nielsen, W. Fundamenski, J. P. Graves, V. Naulin, A. H. Nielsen, and J. J. Rasmussen, Plasma Phys. Controlled Fusion **48**, L1 (2006).
- ⁸⁶W. Fundamenski, O. E. Garcia, and V. Naulin, "Neoclassical dissipation and parallel losses in interchange driven scrape-off layer turbulence" Nucl. Fusion (submitted for publication).
- ⁸⁷S. C. Cowley, H. Wilson, O. Hurrucane, and B. Fong, Plasma Phys. Controlled Fusion **45**, A31 (2003).
- ⁸⁸H. R. Wilson and S. C. Cowley, Phys. Rev. Lett. **92**, 175006 (2004).
- ⁸⁹H. R. Wilson, S. C. Cowley, A. Kirk, and P. B. Snyder, Plasma Phys. Controlled Fusion **48**, A71 (2006).
- ⁹⁰A. Loarte, G. Saibene, R. Sartori *et al.*, Phys. Plasmas **11**, 2668 (2004).